Supporting Information

Anchoring Ru Nanoclusters into Defect-rich Polymeric Carbon Nitride as a Bifunctional Electrocatalyst for Highly Efficient Overall Water Splitting

Jiayang Zhao[a], Haoran Guo[a], Yanyan Li[a], Lirong Zheng[b], Hao Ren[a], Liyun Zhao[a], and Rui Song[a,] *

[a] School of Chemical Sciences, University of Chinese Academy of Sciences, 19 Yuquan Road, Shijingshan District, Beijing, 100049, PR China

[b] Beijing Synchrotron Radiation Facility, Institute of High Energy Physics, Chinese Academy of Sciences, 19 Yuquan Road, Shijingshan District, Beijing, 100049, PR China

*Email: rsong@ucas.ac.cn

Content

1 Experimental Details

1.1 Chemicals and Materials

Urea was purchased from Sinopharm. Ruthenium trichloride ($RuCl_3$), Ru/C (5 wt%), and ethanol were purchased from Shanghai Maclean Biochemical Technology Co., Ltd. Platinum carbon (Pt/C, 20 wt%) was purchased from TKK (Tanaka). Ruthenium oxide (RuO_2) was purchased from Original Equipment Manufacturer (OEM). Nafion solution (DuPont D520) was purchased from Du Pont China Holding Co., Ltd. All reagents received were used without further purification. Deionized water (18.2 MΩ cm) was used in all the experiments.

1.2 Synthesis of g-C_3N_4

The C_3N_4-precursor was prepared by thermal polymerization of urea. In details, 15 g urea was placed in ceramic crucible and then heated at 550 °C for 4 h at a ramp rate of 2.5 °C/min in a muffle furnace. Exfoliated g-C_3N_4 was obtained via thermal exfoliation. To be specific, 0.25 g C_3N_4-precursor was heated at 550 °C under the same heating rate for 5 h.

1.3 Characterization

1) Scanning electron microscopy (SEM) was carried out on a Hitachi SU8220.
2) Transmission electron microscopy (TEM) and energy-dispersive X-ray spectroscopy (EDS) elemental mapping attached to the TEM was performed on an FEI Talos 200X instrument operating an FEG cathode at 200 kV and equipped with the Super-X in-column EDS detector.
3) X-ray diffraction (XRD) was characterized on a Rigaku Smartlab diffractometer with Cu Kα (λ = 1.5406 Å) radiation.
4) The Fourier transform infrared (FT-IR) spectra was recorded with a Vertex 70 spectrophotometer (Bruker Optik GmbH, Germany). The same amount of sample is taken during the test.
5) UV-vis diffuse reflectance spectra were acquired by a spectrophotometer (UV-3600Plus) and $BaSO_4$ was used as the reflectance standard.
6) Electron paramagnetic resonance (EPR) was measured by an A300-10/12 of Bruker, Germany.

7) The inductively coupled plasma optical emission spectrometry was conducted on Agilent ICPOES730.
8) The elemental analysis was measured on a vario UNICUBE elementar.
9) X-ray photoelectron spectra (XPS) were measured by a Thermo Scientific ECSALab 250Xi X-ray photoelectron spectrometer with an Al Kα X-ray radiation (1486 eV).
10) Nitrogen absorption/desorption isotherms were measured on a Micromeritics ASAP2460 instrument and after the samples were degassed about 24 h at 60 °C and the specific surface areas were calculated by the Brunauer-Emmett-Teller (BET) method.
11) The X-ray absorption find structure data were collected at 1W1B station in Beijing Synchrotron Radiation Facility (BSRF). The storage rings of BSRF were operated at 2.5 GeV with a maximum current of 250 mA.

1.4 Electrochemical Measurements

All the electrochemical measurements were conducted in a standard three-electrode setup on CHI 660E electrochemical workstation (Chenhua Instruments, Shanghai, China), using carbon papers electrode modified with catalysts as a working electrode, a graphite rod as counter electrode and Hg/HgO (filled in 1 M KOH) electrode as reference electrode. For the preparation of catalyst inks, 5 mg catalysts were dispersed in the mixture of 650 μL C_2H_6O and 300 μL H_2O by sonicating for 40 min. Then the 50 μL Nafion solution was added in the solution, and sonicated for 20 min. Afterwards, the 150 μL homogeneous suspension was drop onto carbon papers electrode where the total effective loading surface area is 0.25 cm^2, and the mass loading is 3.0 mg cm^{-2}.

Multiple cyclic voltammetry (CV) scans were firstly performed at a scan rate of 10 mV s^{-1} until reached a stable state of electrodes. Then, linear sweep voltammetry (LSV) was conducted with a scan rate of 2 mV s^{-1} in 1 M KOH solution. The electrochemical impedance spectroscopy (EIS) measurements were carried out at different overpotential for HER and OER over a frequency range from 100 kHz to 0.01 Hz with an amplitude of 10 mV. The long-term stability was tested by chronopotentiometry and muti-current steps. All the polarization curves were corrected using 90% iR compensation. Potentials were referenced to the reversible hydrogen electrode (RHE): $E_{(RHE)} = E_{(Hg/HgO)} + 0.098 + 0.059$ pH. The overpotential

(η) was calculated according to the following equation: $\eta_{(HER)} = E_{(RHE)} - 0$ V; $\eta_{(OER)} = E_{(RHE)} - 1.23$ V.

1.4.1 Calculation of C_{dl} and ECSA

The double layer capacitance (C_{dl}) of all catalysts was estimated in non-Faradaic potential windows and calculated by plotting $(J_a-J_c)/2$ versus the scan rate V_s, where j_a and j_c are the anodic and cathodic current density using the equation:

$$C_{dl} = \frac{\nabla Q}{\nabla V} = \frac{J_a - J_c}{v} \quad (1.)$$

The electrochemically active surface area (ECSA) of the material can be calculated by dividing C_{dl} by the specific capacitance (C_s) of the material:

$$ECSA = \frac{C_{dl}}{C_s} \quad (2.)$$

Where C_s is the specific capacitance, chosen as $C_s = 0.040$ mF cm^{-2} in 1 M KOH based on reported values.

1.4.2 Calculation of ESA_{CO}

CO stripping experiment was carried out with the method reported by Gasteiger et al.[1, 2, 3] In detail, CO adsorption was conducted in 1 M KOH with CO bubbling for 20 min. After equilibrated for 10 min, the electrolyte was saturated with nitrogen by bubbling nitrogen for 30 min. During all the above processes, the potential was held at 0.1 V. Then the CV curves were collected positively from the adsorption potential of 0.1 V, then within the range of 0~1 V (vs. RHE) at a scan rate of 10 mV s^{-1}. According to the results of CO stripping, ESA_{CO} value of Ru NCs/V_N-C_3N_4 were determined by assuming that the electrooxidation of one CO* monolayer required a charge density of 420 μC cm_{Ru}^{-2}.[4, 5]

1.4.3 Calculation of TOF

The TOF value was calculated according to the previous report, and the detail was described as below (Take Ru NCs/V_N-C_3N_4 as an example):

$$\text{TOF} = \frac{Total\ Hydrogen\ turnovers\ /\ geometric\ area}{Active\ sites\ /\ geometric\ area} \quad (3.)$$

The number of total hydrogen turnovers was calculated from the current density derived from the LSV curve according to the following equation:

Total oxygen turnovers

$$= (|j|\ mA/cm^2)\left(\frac{1\ C/s}{1000\ mA}\right)\left(\frac{1\ mol\ e^-}{96485\ C}\right)\left(\frac{1\ mol}{4\ mol\ e^-}\right)\left(\frac{6.02\times\ 10^{23} moleculrs\ O_2}{1\ mol\ O_2}\right)$$

$$= 1.560\times10^{15}\ O_2/s\ cm^2\ per\ mA/cm^2 \quad (4.)$$

The number of active sites in Ru NCs/V_N-C_3N_4, $RuCl_x$-C_3N_4, commercial Ru/C and RuO_2 catalysts were calculated from the mass loading on the work electrode. The Ru atomic weight was determined by ICP data, assuming each Ru center accounts for one active site:

The number of active sites

$$= \left(\frac{catalyst\ loading\ per\ geometric\ area\ (g/cm^2)\ \times Ru\ wt\%}{101.07\ g/mol}\right)\left(\frac{6.02\times\ 10^{23} Ru\ atoms}{1\ mol\ Ru}\right)$$

$$= \left(\frac{3.0\ \times\ 10^{-3}\ (g/cm^2)\ \times 5.572 wt\%}{101.07\ g/mol}\right)\left(\frac{6.02\times\ 10^{23} Ru\ atoms}{1\ mol\ Ru}\right)$$

$$= 9.956\times10^{17}\ Ru\ sites\ per\ cm^2 \quad (5.)$$

Finally, the current density value of LSV polarization curve under different overpotential is substituted into equation S3 to obtain TOF:

$$\text{TOF} = \left(\frac{1.560\times10^{15}}{9.956\times10^{17}}\times\ |j|\right) = 0.001566\times\ |j|$$

1.4.4 Calculation of mass activity

The mass activities of Ru NCs/V_N-C_3N_4, $RuCl_x$-C_3N_4, commercial Ru/C and RuO_2 catalysts were calculated at the overpotential of 100 mV (for HER) and the potential of 1.60 V (for OER), normalized to the Ru loadings. The mass activities of commercial Pt/C for HER and OER were normalized to the Pt loading. Detail was described as below (Take Ru NCs/V_N-C_3N_4 as an example):

$$\text{Mass activity} = \frac{Current\ density\ (mA/cm^2)}{catalyst\ loading\ per\ geometric\ area\ (mg/cm^2)\ \times Ru\ wt\%} \quad (6.)$$

For HER process:

$$\text{Mass activity} = \frac{448.9\ (mA/cm^2)}{3.0\ (mg/cm^2)\ \times 5.572wt\%} = 2685.5\ \text{A/g} \qquad (7.)$$

For OER process:

$$\text{Mass activity} = \frac{401.0\ (mA/cm^2)}{3.0\ (mg/cm^2)\ \times 5.572wt\%} = 2398.9\ \text{A/g} \qquad (8.)$$

1.5 XAFS Analysis

The acquired EXAFS data were processed according to the standard procedures using the ATHENA module implemented in the IFEFFIT software packages. The k^3-weighted EXAFS spectra were obtained by subtracting the post-edge background from the overall absorption and then normalizing with respect to the edge-jump step. Subsequently, k^3-weighted $\chi(k)$ data of Fe K-edge were Fourier transformed to real (R) space using a hanning windows (dk=1.0 $Å^{-1}$) to separate the EXAFS contributions from different coordination shells. To obtain the quantitative structural parameters around central atoms, least-squares curve parameter fitting was performed using the ARTEMIS module of IFEFFIT software packages.[6, 7, 8]

1.6 DFT Calculation

First-principles calculations were performed within the density functional theory framework.[9] The projector-augmented wave (PAW) method [10, 11] and the generalized gradient approximation (GGA) [12] for the exchange-correlation energy functional, as implemented in the Vienna ab initio simulation package (VASP) [13, 14, 15] were used. The GGA calculation was performed with the Perdew-Burke-Ernzerhof (PBE) [16] exchange-correlation potential. Considered long-range interaction between molecules/intermediates and surface, Van der Waals interactions were considered using DFT-D3 correlation.[17] To avoid effects come from other slabs, a vacuum of 15 Å was added along z direction. The convergence criterion of geometry relaxation was set to 0.01 eV•$Å^{-1}$ in force on each atom. The energy cutoff for plane wave-basis was set to 500 eV. The K points were sampled with 3×3×1 by Monkhorst-Pack method.

Free energies of each reaction steps were calculated as $G = E_{DFT} + E_{ZPE} - T\Delta S$, where E_{DFT} is the DFT calculated energy, E_{ZPE} and $T\Delta S$ are calculated by DFT vibration frequency calculations.

For HER, the hydrogen adsorption free energy (ΔG_{H*}) was calculated by the following equation:[18]

$$\Delta G_{H*} = \Delta E_{H*} + 0.24\ \text{eV} \quad (9.)$$

Where ΔE_{H*} is defined by the following equation:

$$\Delta E_{H*} = E_{H*} - (E_{*} + 1/2E_{H_2}) \quad (10.)$$

Where E_{H*} is the total energy of H atom on the support, E_{*} is the total energy of support, E_{H_2} is the energy of the gas H_2 calculated by setting the isolated H_2 in a box of 10.0 Å×10.0 Å×10.0 Å. The Gibbs free energy for the well-known highly efficient Pt catalyst is near-zero as $|\Delta G_{ads}| \approx 0.09$ eV.[19]

For OER, the Gibbs free energy was calculated by the generally reported four electrons process:

$$OH^- + * \rightarrow *OH + e^- \quad (11.)$$

$$OH^- + *OH \rightarrow *O + H_2O\ (l) \quad (12.)$$

$$*O + OH^- \rightarrow *OOH + e^- \quad (13.)$$

$$*OOH + OH^- \rightarrow O_2 + H_2O\ (l) + e^- \quad (14.)$$

Where * represents an adsorption site on the catalyst, and *OH, *O and *OOH denote the corresponding adsorbed intermediates. Also, at standard conditions, the free energies change for all OER electrochemical steps ($\Delta G_{1\text{-}4}$) can be expressed as:

$$\Delta G_1 = \Delta G_{*OH} \quad (15.)$$

$$\Delta G_2 = \Delta G_{*O} - \Delta G_{*OH} \quad (16.)$$

$$\Delta G_3 = \Delta G_{*OOH} - \Delta G_{*O} \quad (17.)$$

$$\Delta G_4 = 4.92 - \Delta G_{*OOH} \quad (18.)$$

Therefore, the theoretical overpotential η was obtained according to the equation:

$$\eta = \max\ [\Delta G_1, \Delta G_2, \Delta G_3, \Delta G_4]/e - 1.23\ \text{V} \quad (19.)$$

The change in free energy (ΔG) of per reaction step was calculated as following:[20]

$$\Delta G = \Delta E + \Delta ZPE - T\cdot\Delta S + \Delta G_U + \Delta G_{pH} \quad (20.)$$

Where ΔE is the change of the total reaction energy obtained from DFT calculation, ΔZPE is the change of the zero-point energy, T is the temperature (300 K), and ΔS is

the change of the entropy. ΔG_U = -eU, where U is the potential at the electrode and e is the transferred charge. ΔG_{pH} = $k_B \cdot T \times \ln 10 \times pH$, where k_B is the Boltzmann constant and T = 300 K. In this work, the influence of pH was neglected. The free energy of O_2 is obtained from the reaction $O_2 + 2H_2 \rightarrow 2H_2O$, which is 4.92 eV at 300 K and a pressure of 0.035 bar. The free energy of OH^- is defined as $G(H_2O)$-$G(H^+)$, and the free energy of H^+ is equal to $1/2H_2$. The entropies of molecules (including O_2, H_2, and H_2O, etc.) in the gas (or liquid) phase are taken from the "CRC Handbook of Chemistry and Physics".[21]

The d-band center was calculated based on the following equation:

$$\varepsilon_d = \frac{\int_{-\infty}^{\infty} \rho(x) x dx}{\int_{-\infty}^{\infty} \rho(x) dx} \quad (21.)$$

Where $\rho(x)$ is the PDOS at the energy of x.

2 Results and Discussion

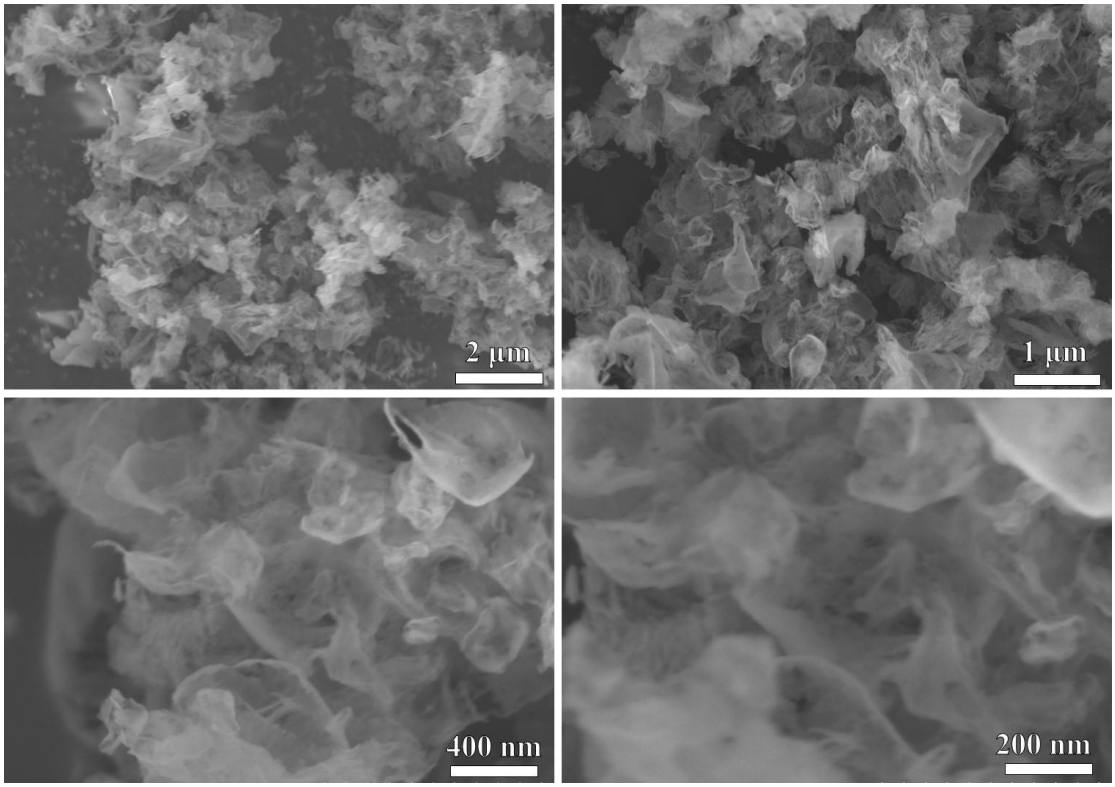

Fig. S1 SEM images of g-C_3N_4 at different magnifications.

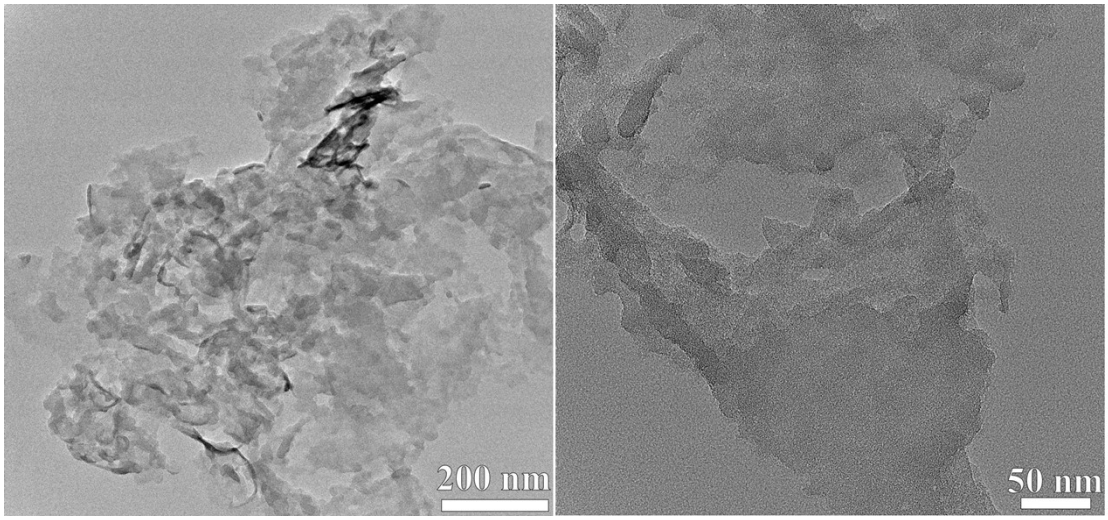

Fig. S2 TEM images of g-C_3N_4 at different magnifications.

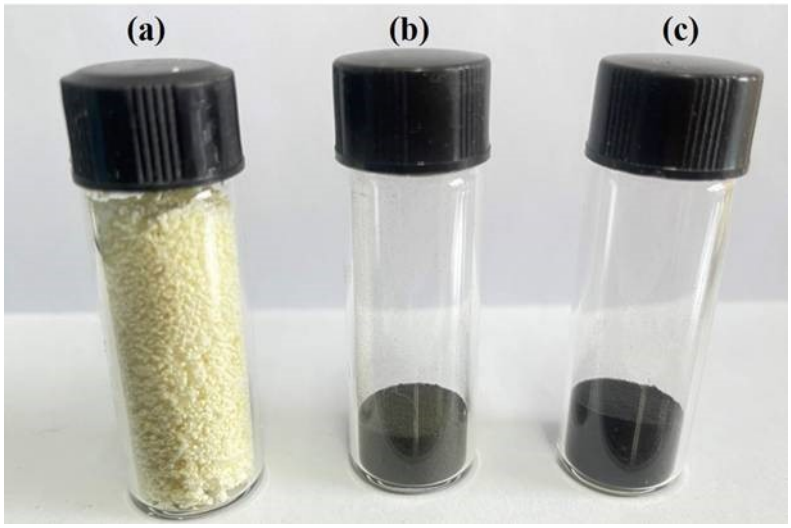

Fig. S3 Photographs of (**a**) g-C_3N_4, (**b**) $RuCl_x$-C_3N_4, and (**c**) Ru NCs/V_N-C_3N_4.

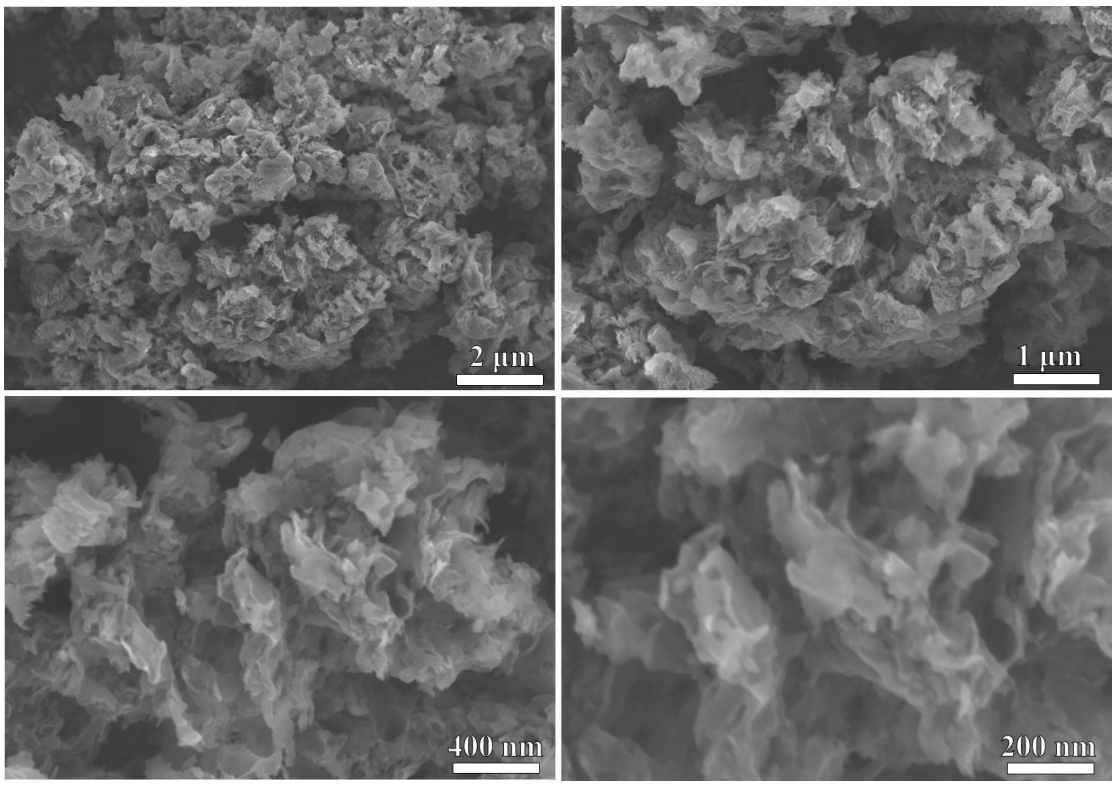

Fig. S4 SEM images of $RuCl_x$-C_3N_4 at different magnifications.

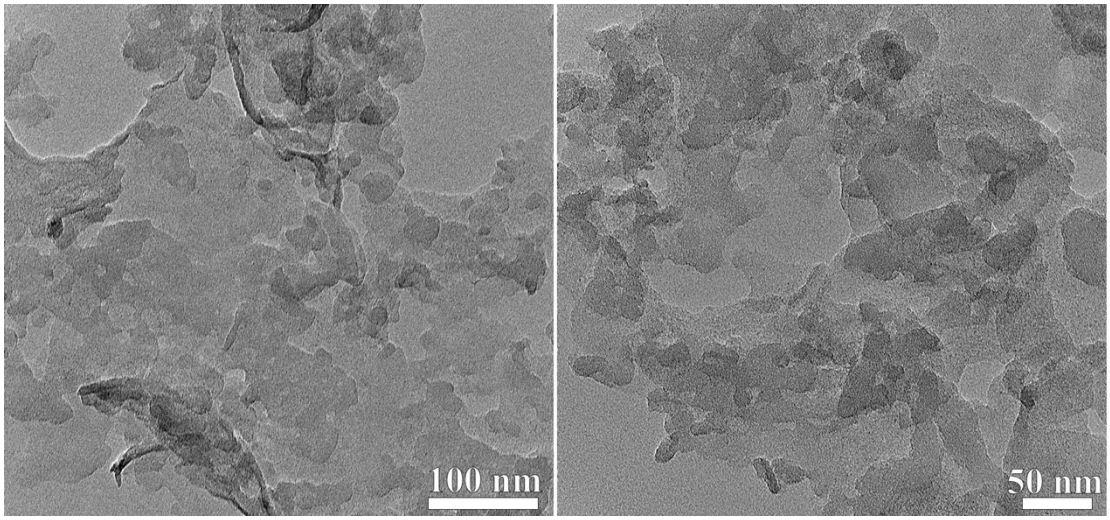

Fig. S5 TEM images of $RuCl_x$-C_3N_4 at different magnifications.

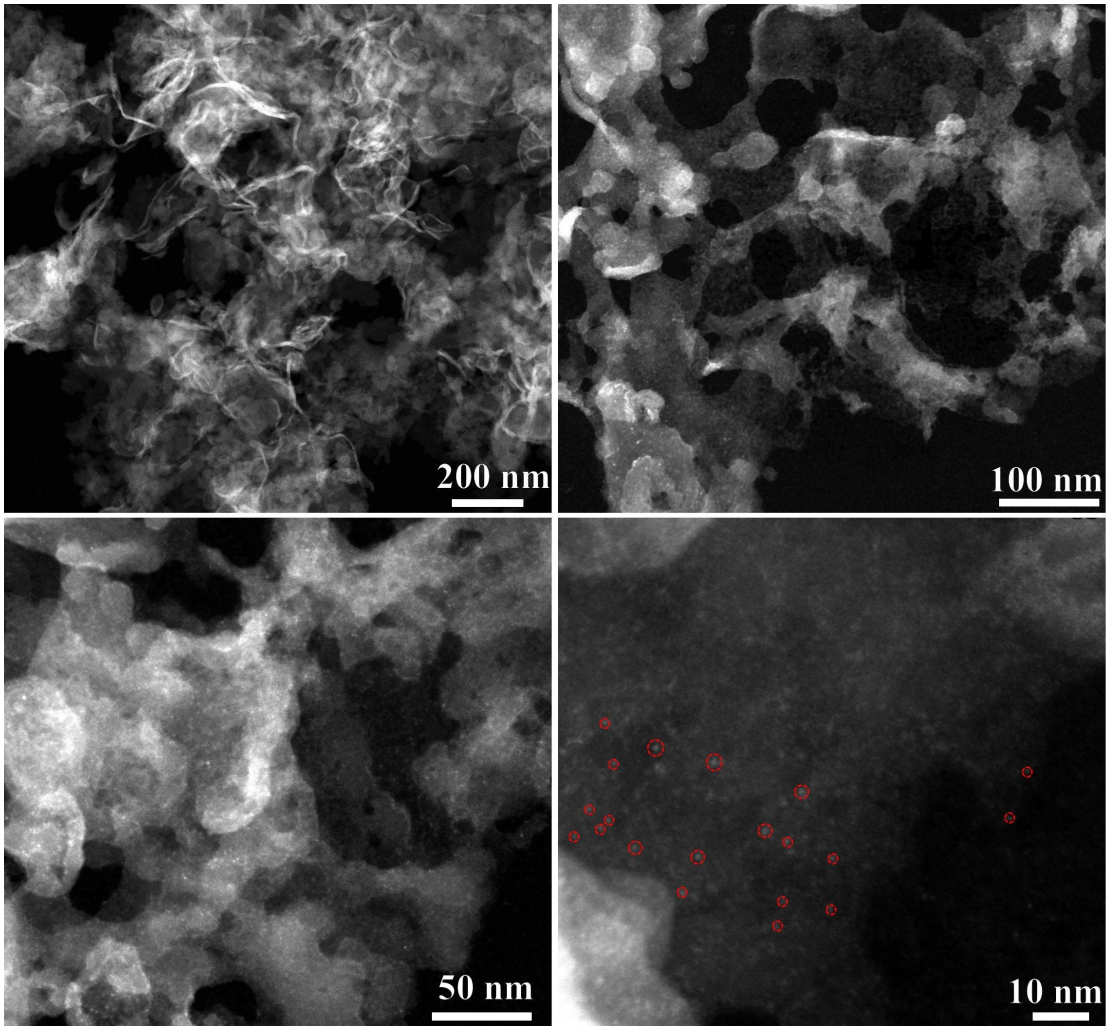

Fig. S6 HAADF-STEM images of $RuCl_x$-C_3N_4.

Each bright spot (as shown in the red circles) represents Ru nano-species that are evenly dispersed in the carbon matrix without aggregating.

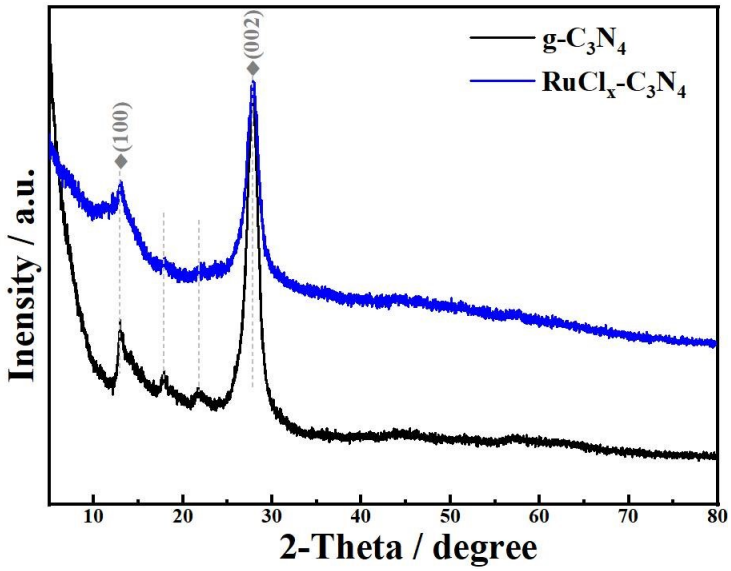

Fig. S7 XRD patterns of the g-C_3N_4 and $RuCl_x$-C_3N_4.

The g-C_3N_4 and $RuCl_x$-C_3N_4 manifests similar X-ray diffraction (XRD) patterns with two diffraction peaks at 13.0° and 27.4°, corresponding to the (100) and (002) planes of g-C_3N_4, respectively (**Fig. S7**).[22] Noting that no obvious peak of Ru species was detected for $RuCl_x$-C_3N_4 due to the small size of Ru nano-species.

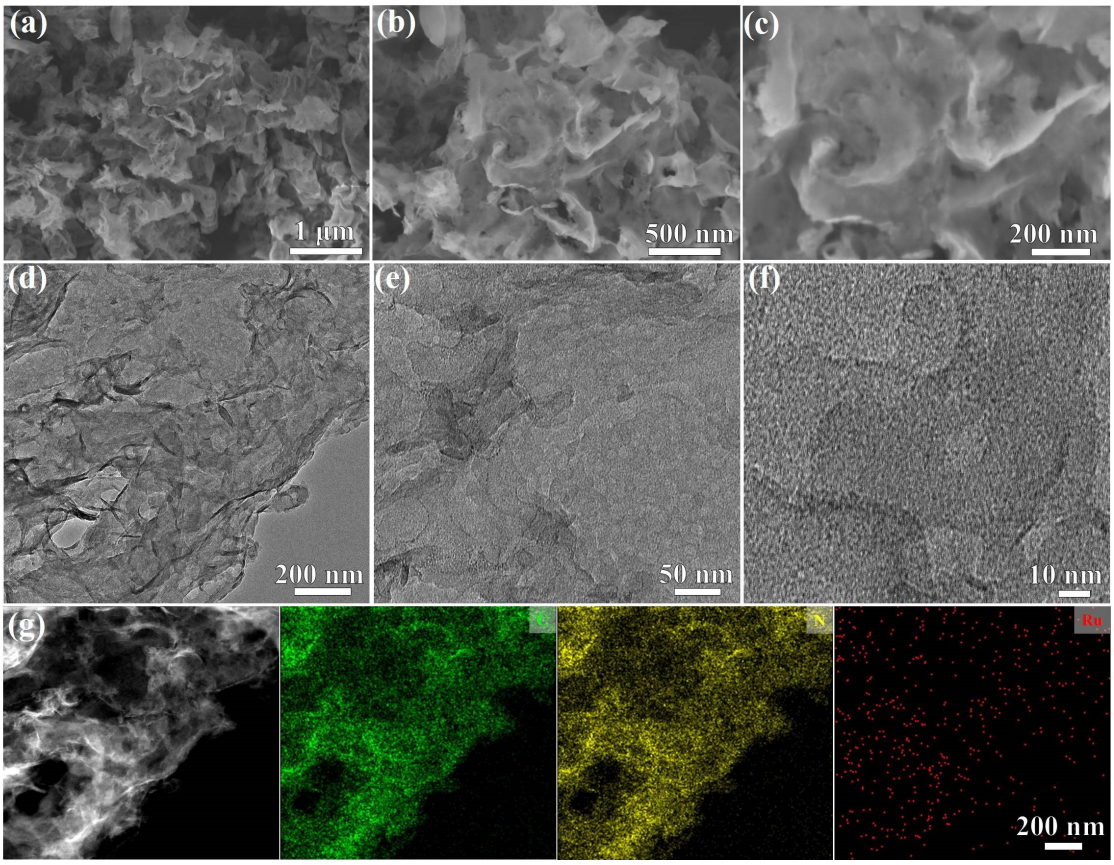

Fig. S8 (**a**)-(**c**) SEM images and (**d**)-(**f**) TEM images of $RuCl_x$-C_3N_4-350 °C at different magnifications. (**g**) HAADF-STEM image of $RuCl_x$-C_3N_4-350 °C and the EDS mapping of Ru, C and N.

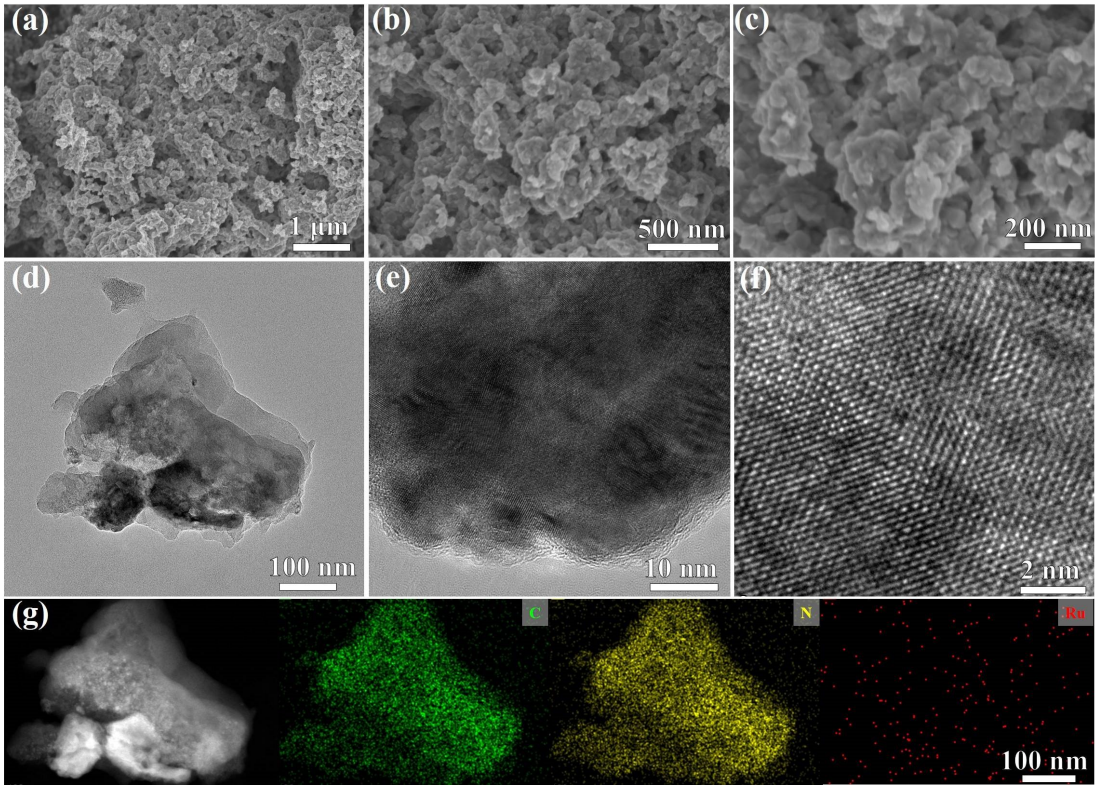

Fig. S9 (**a**)-(**c**) SEM images, (**d**) TEM image and (**e**)-(**f**) HRTEM images of $RuCl_x$-C_3N_4-550 °C at different magnifications. (**g**) HAADF-STEM image of $RuCl_x$-C_3N_4-550 °C and the EDS mapping of Ru, C and N.

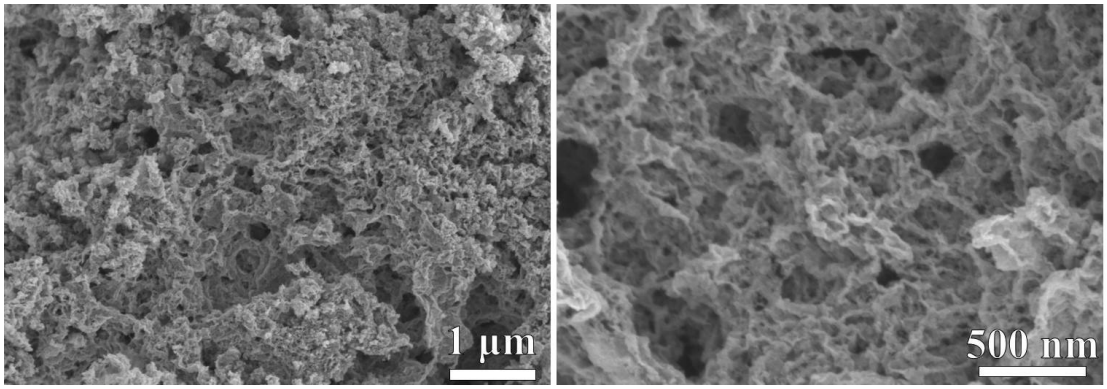

Fig. S10 SEM images of $RuCl_x$-C_3N_4-450 °C at different magnifications.

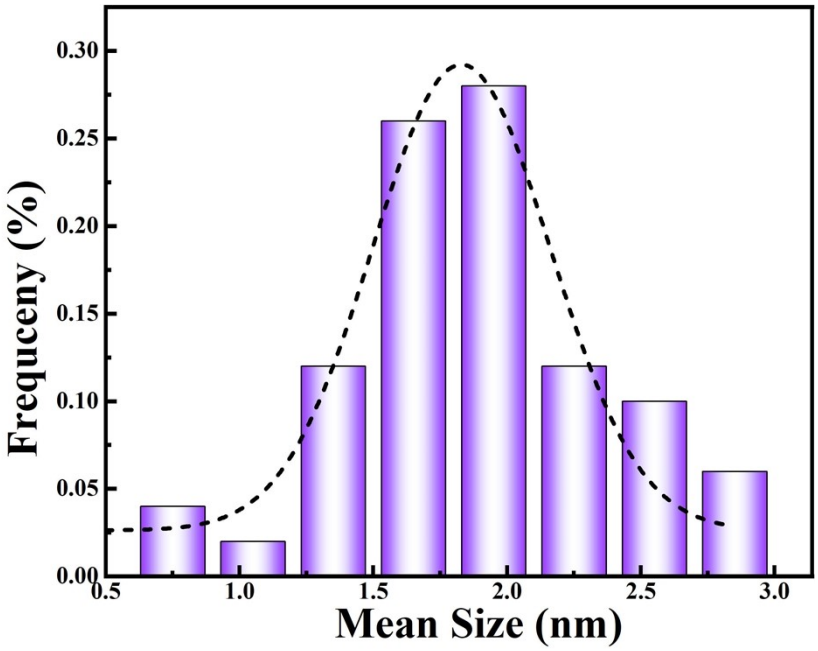

Fig. S11 The size statistics of nanoparticles in region I.

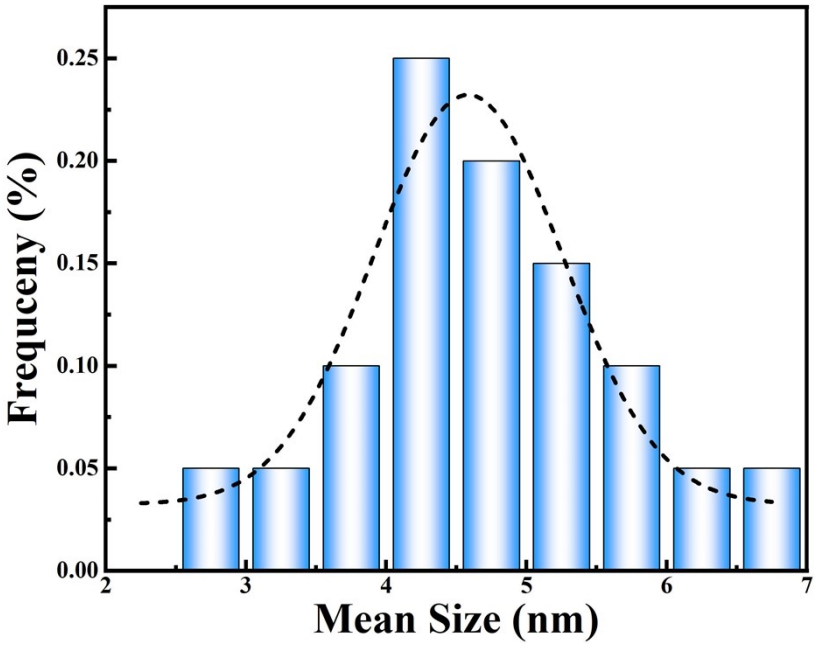

Fig. S12 The size statistics of nanoparticles in region II.

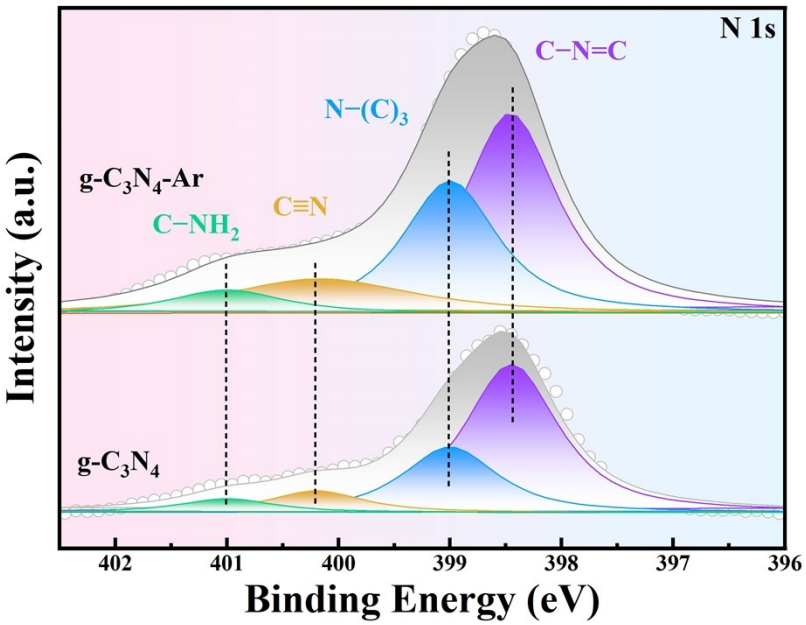

Fig. S13 High-resolution XPS spectra of N 1s for g-C_3N_4 and g-C_3N_4-Ar.

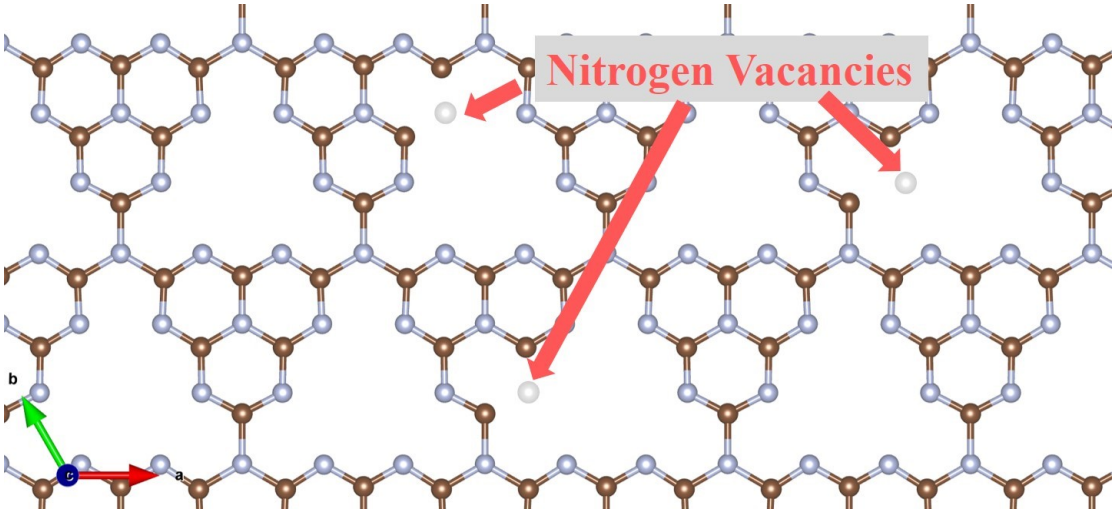

Fig. S14 Schematic illustration for nitrogen vacancies at the pyridinic nitrogen sites.

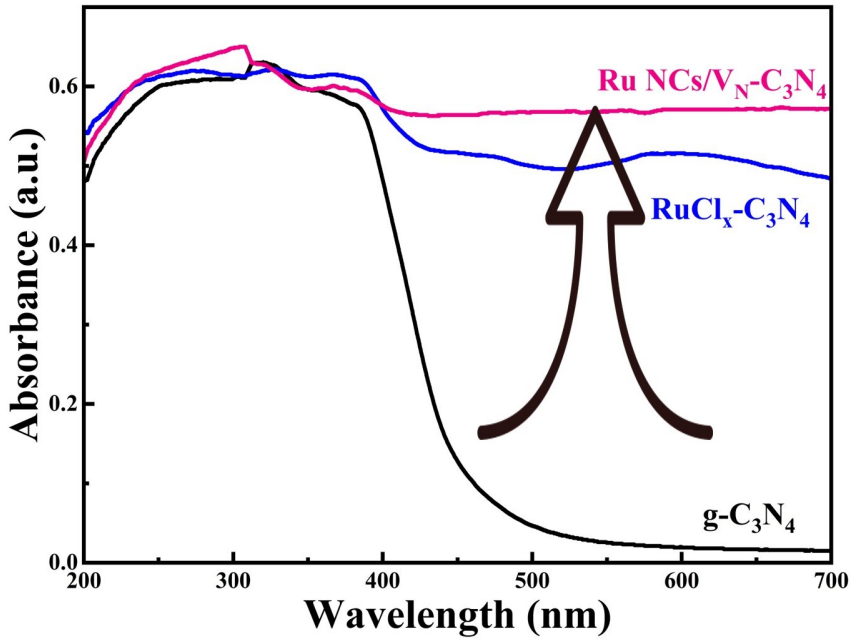

Fig. S15 UV-Vis diffuse reflection spectra of g-C_3N_4, $RuCl_x$-C_3N_4 and Ru NCs/V_N-C_3N_4.

It is noteworthy that the color of g-C_3N_4 is yellow, whereas the color changes to greenish-brown and black for $RuCl_x$-C_3N_4 and Ru NCs/V_N-C_3N_4. These color changes are consistent with the much wider and stronger absorption spectra. For g-C_3N_4, the absorption band typically appears in the blue part of the visible region. When incorporating into Ru species, the absorption band of $RuCl_x$-C_3N_4 at the visible wavelength region was significantly enhanced, which corroborates the destabilization of the stable conjugated π electron network of the C_3N_4 framework, implying the interactive reaction toward C_3N_4 and Ru species. After annealing, the absorption band of Ru NCs/V_N-C_3N_4 at 400-700 nm was further enhanced, suggesting the formation of abundant V_N was beneficial to increase π electron transition and delocalization in the conjugated system.

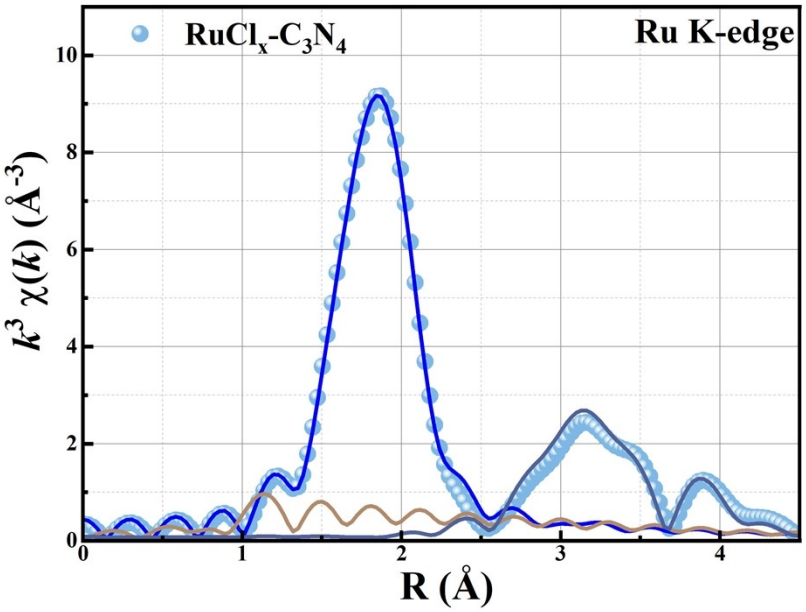

Fig. S16 First-shell fitting of EXAFS spectra of $RuCl_x$-C_3N_4.

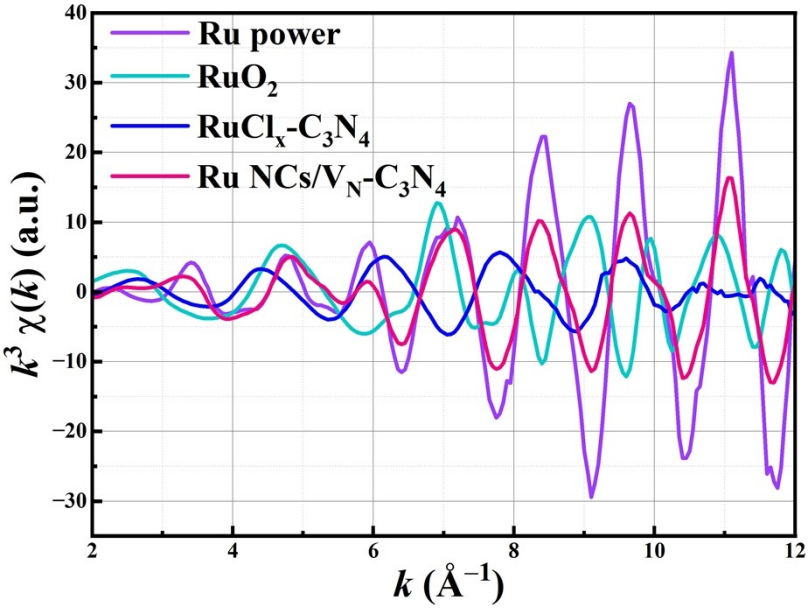

Fig. S17 Ru K-edge EXAFS of oscillations.

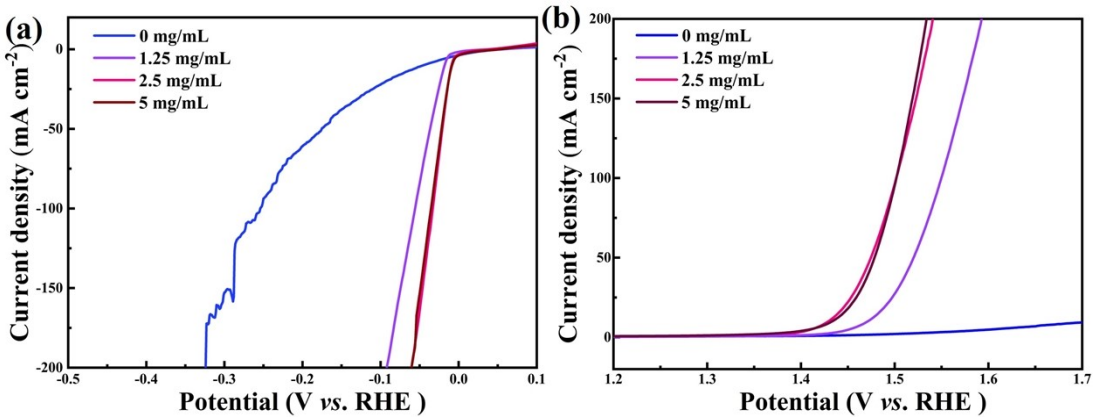

Fig. S18 LSV curves of samples with $RuCl_3$ solution in different concentrations.

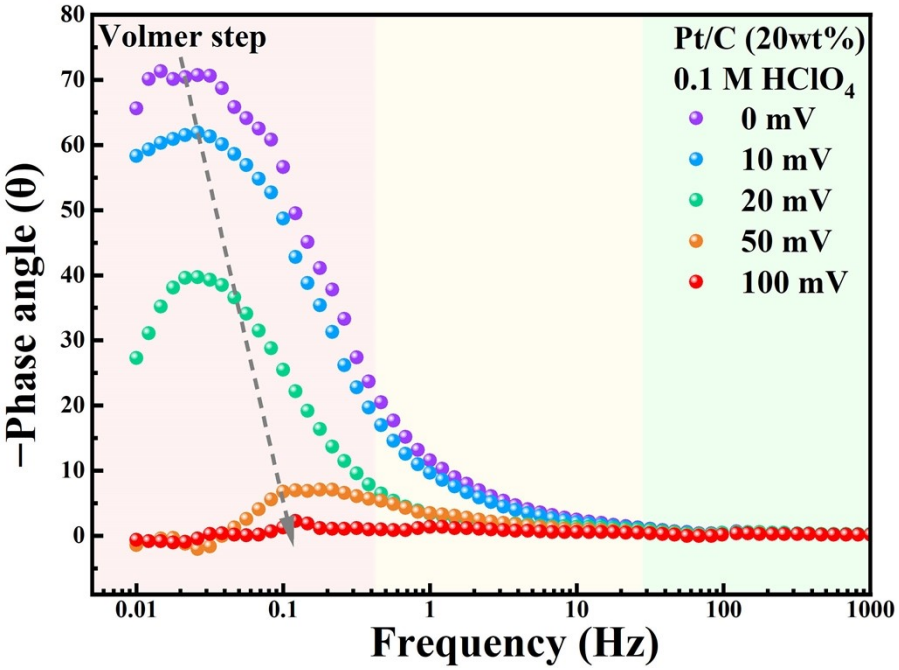

Fig. S19 Operando Bode plots of commercial Pt/C at various overpotential in 0.1 M $HClO_4$.

Volmer step: $H_3O^+ + e^- \rightleftharpoons H_{ad} + H_2O$

Tafel step: $2H_{ad} \rightleftharpoons H_2$

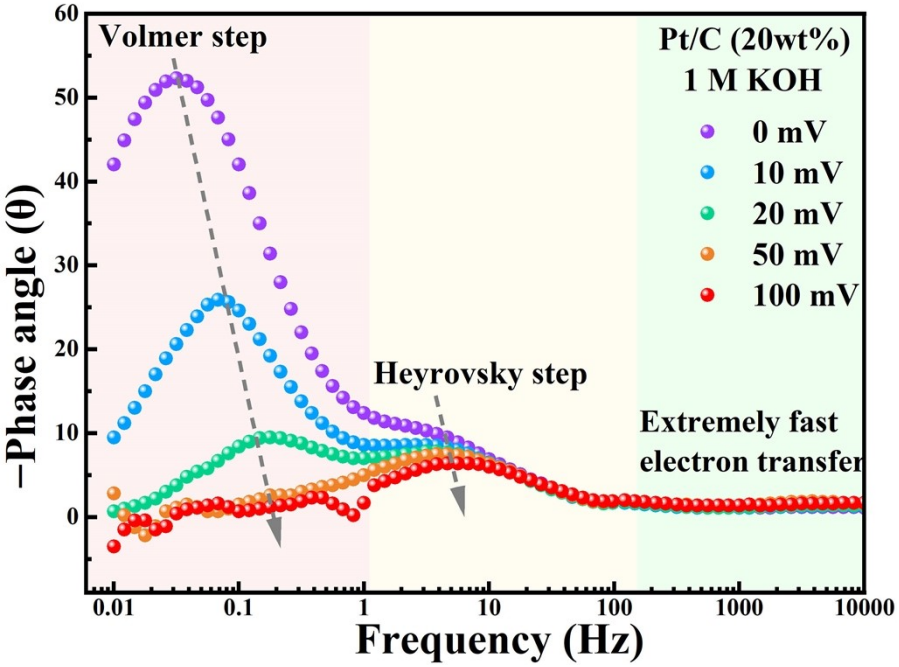

Fig. S20 Operando Bode plots of commercial Pt/C at various overpotential in 1 M KOH.

The phase angle reduced quickly at the low-frequency region, and decreased tardily at the middle-frequency region, meaning the Volmer-Heyrovsky mechanism of Pt/C with Heyrovsky step as RDS.

Volmer step: $H_3O^+ + e^- \rightleftharpoons H_{ad} + H_2O$

Heyrovsky step: $H_{ad} + H_3O^+ + e^- \rightleftharpoons H_2 + H_2O$

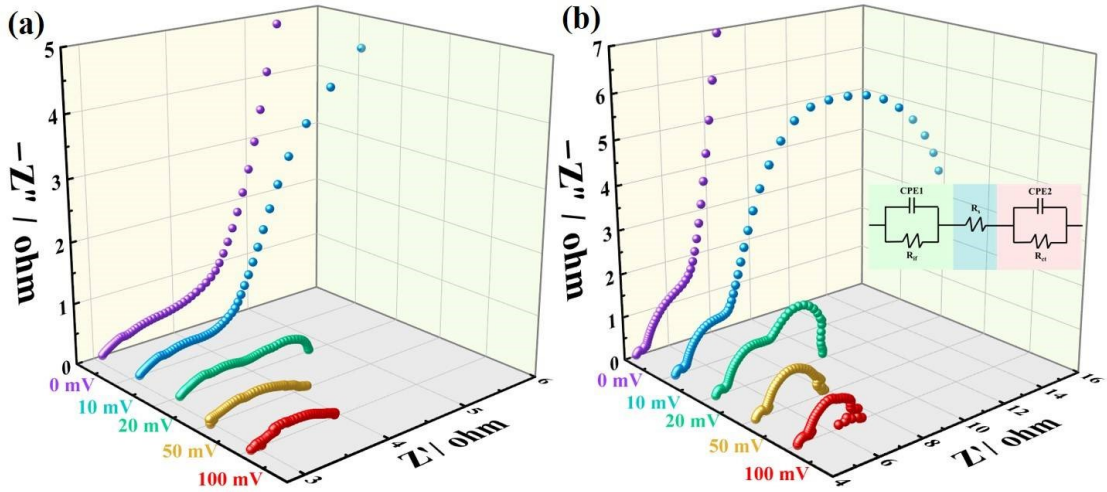

Fig. S21 Operando Nyquist plots of (**a**) Ru NCs/V_N-C_3N_4 and (**b**) Pt/C at various voltages in 1 M KOH. The inset was equivalent circuit.[23]

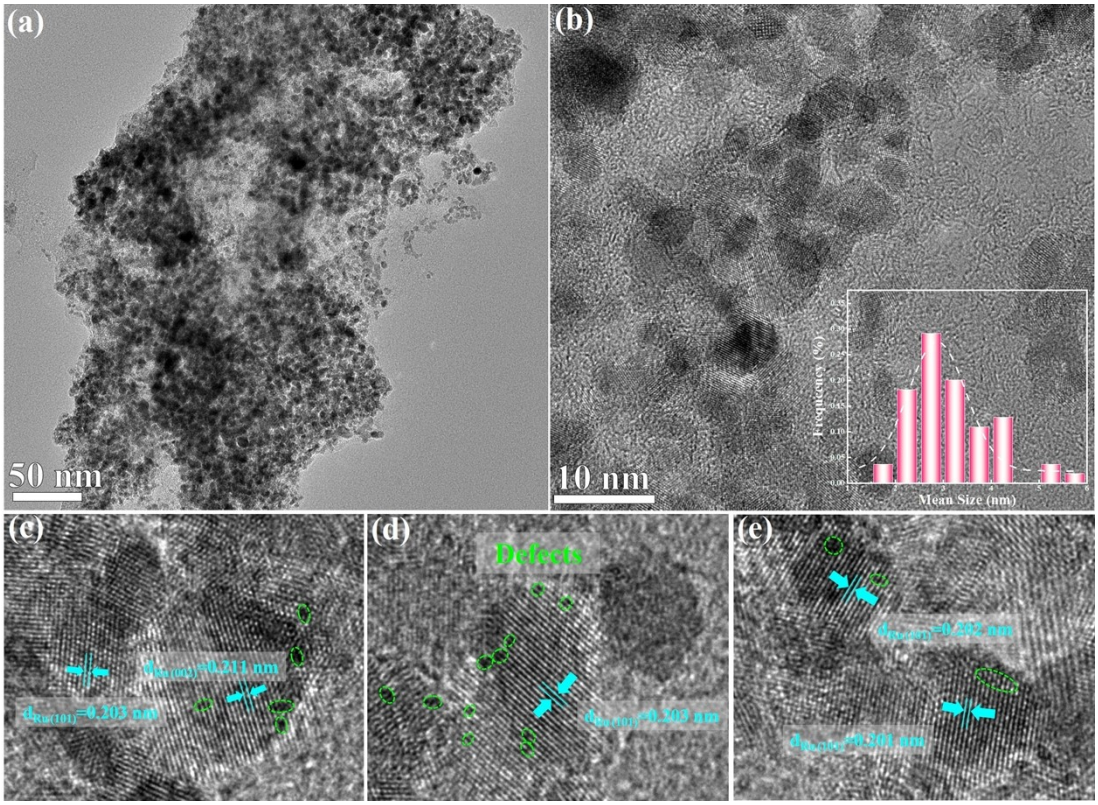

Fig. S22 (**a**) TEM and (**b**-**e**) HRTEM images of Ru NCs/V_N-C_3N_4 after long-term HER stability test.

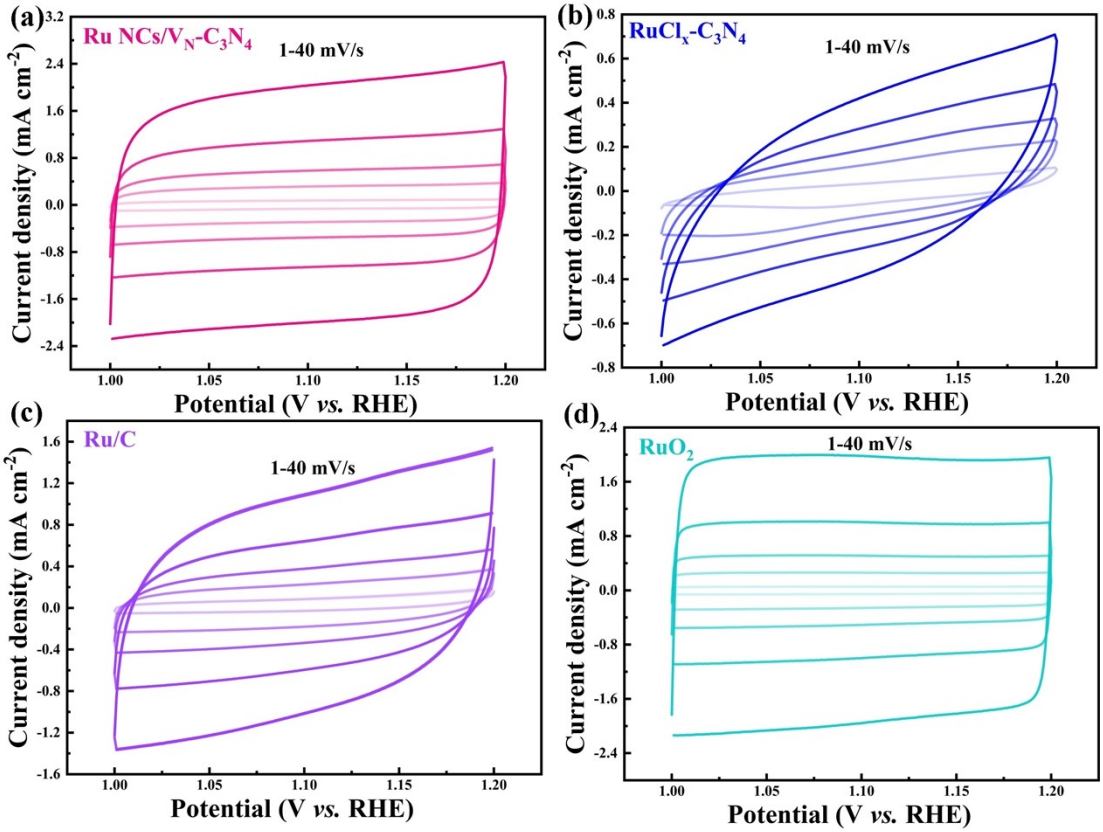

Fig. S23 CV curves of (**a**) Ru NCs/V_N-C_3N_4, (**b**) $RuCl_x$-C_3N_4, (**c**) Ru/C, and (**d**) RuO_2 at varying scan rates (1, 5, 10, 20 ,40 mV s^{-1}).

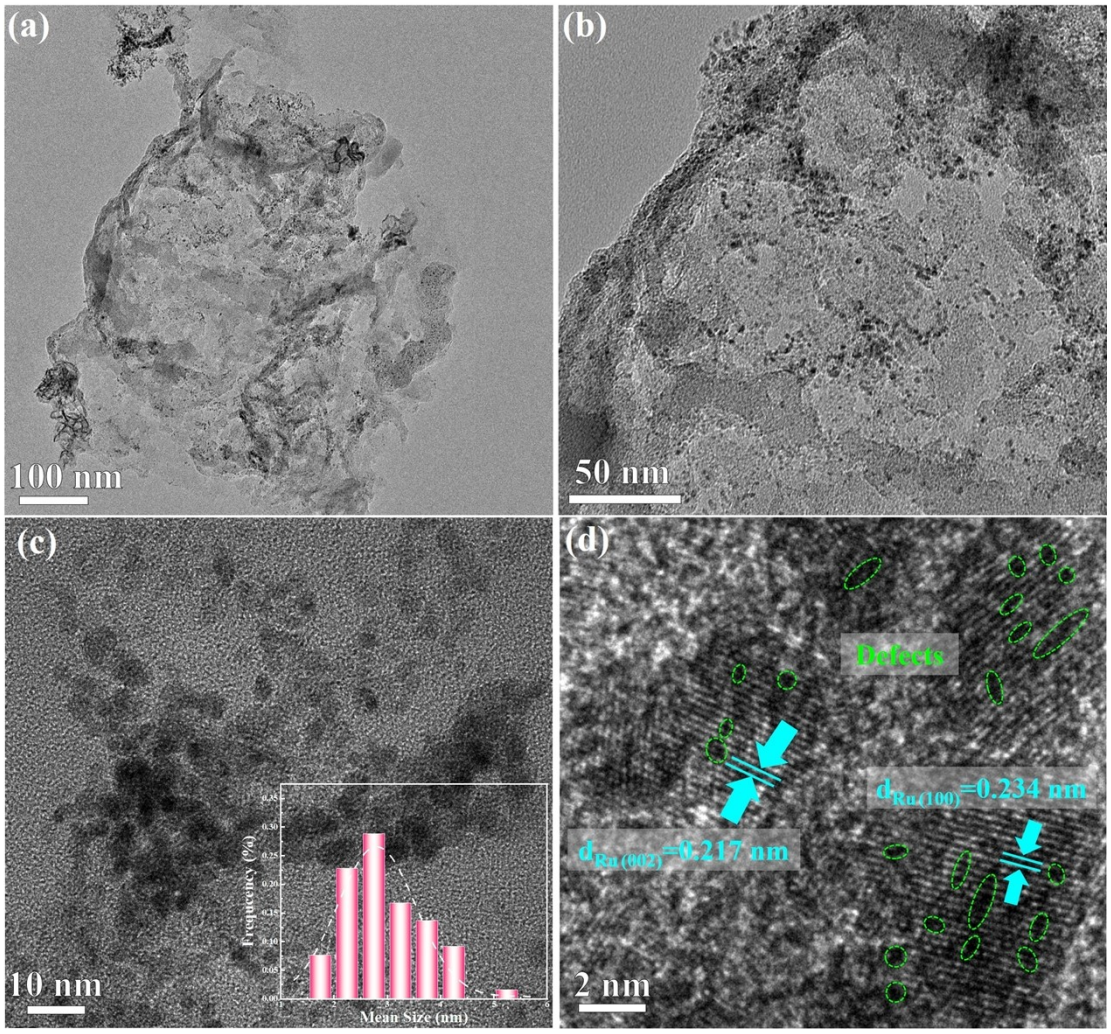

Fig. S24 (**a**-**b**) TEM and (**c**-**d**) HRTEM images of Ru NCs/V_N-C_3N_4 after long-term OER stability test.

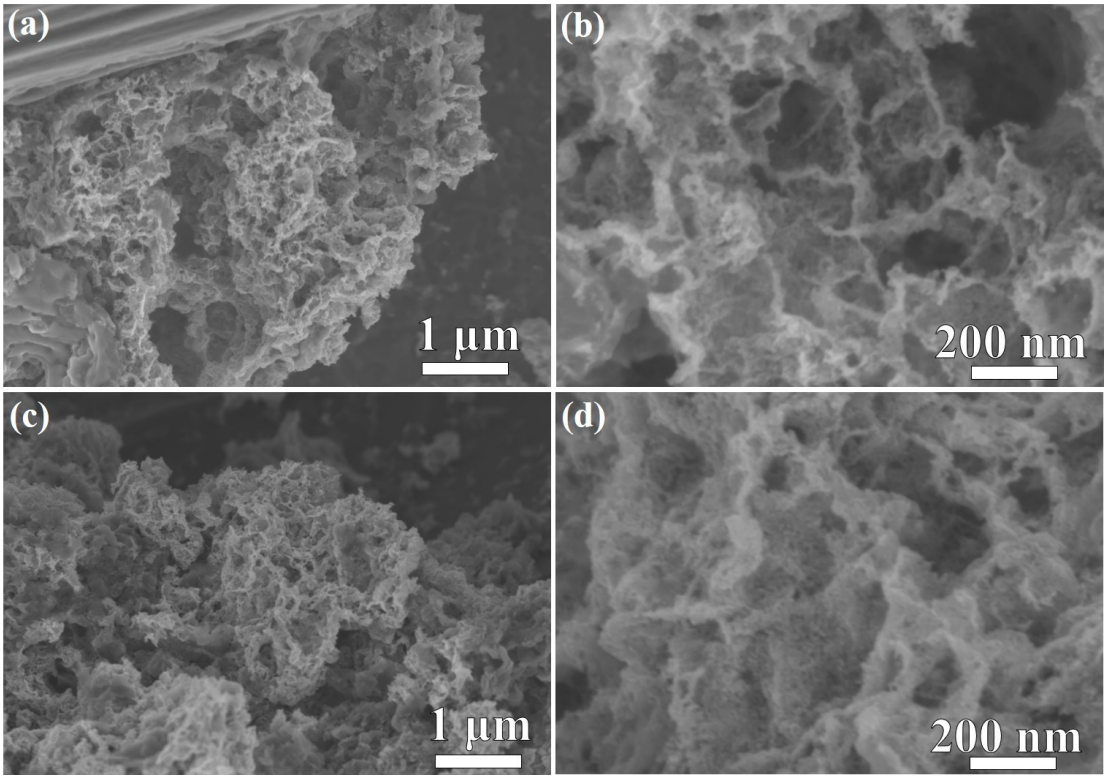

Fig. S25 (**a**-**b**) SEM images of Ru NCs/V_N-C_3N_4 at cathode after long-term electrolysis. (**c**-**d**) SEM images of Ru NCs/V_N-C_3N_4 at anode after long-term electrolysis.

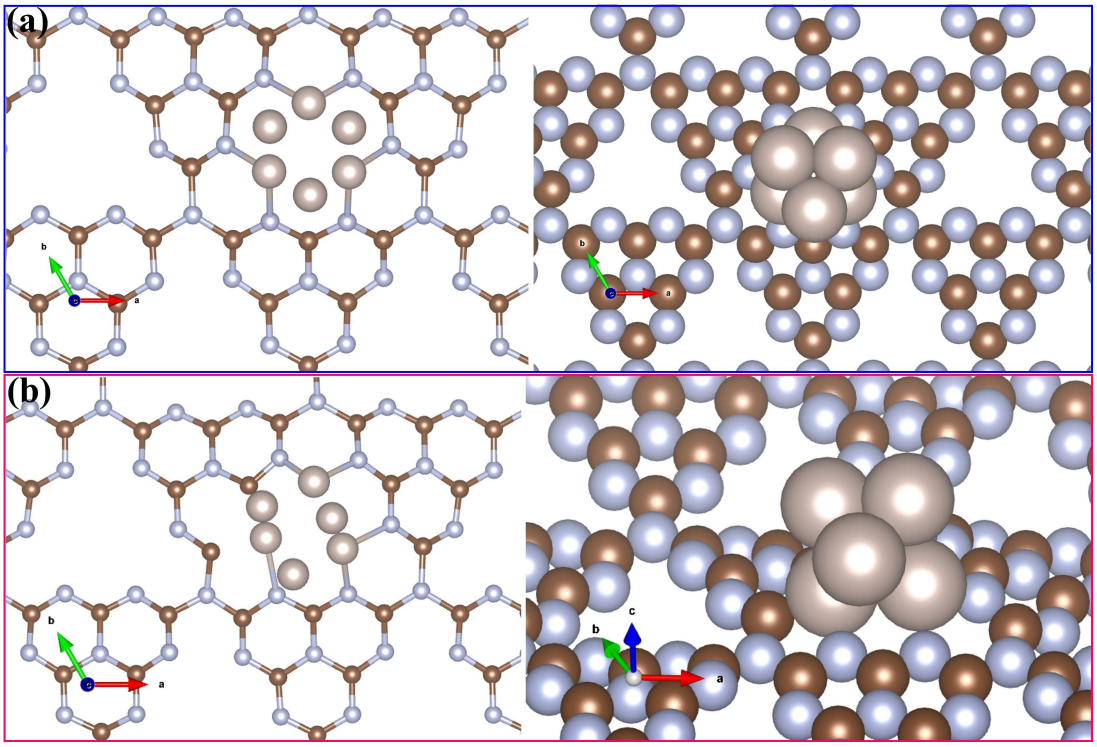

Fig. S26 The structure model for (**a**) Ru NCs/C_3N_4 and (**b**) Ru NCs/V_N-C_3N_4.

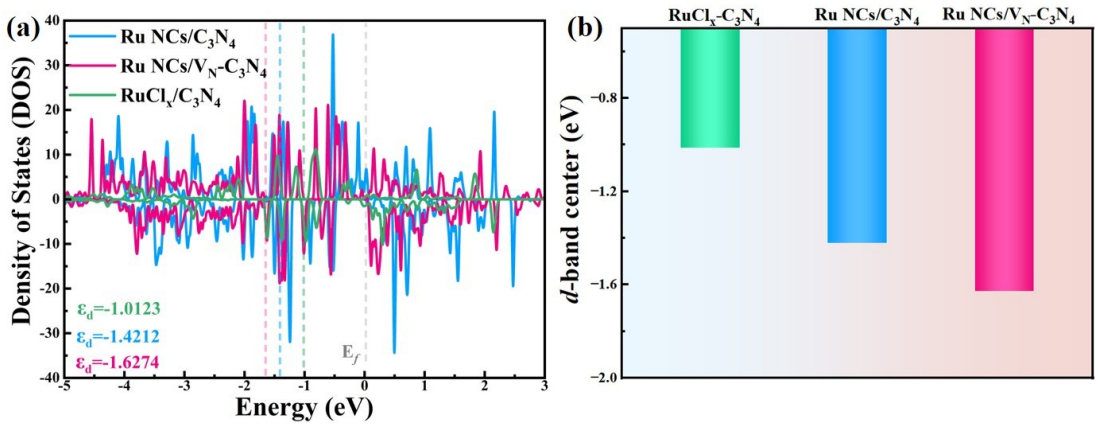

Fig. S27 (**a**) Calculated partial DOS of Ru NCs/V_N-C_3N_4, Ru NCs/C_3N_4 and $RuCl_x$-C_3N_4. (**b**) Calculated *d*-band center of Ru NCs/V_N-C_3N_4, Ru NCs/C_3N_4 and $RuCl_x$-C_3N_4.

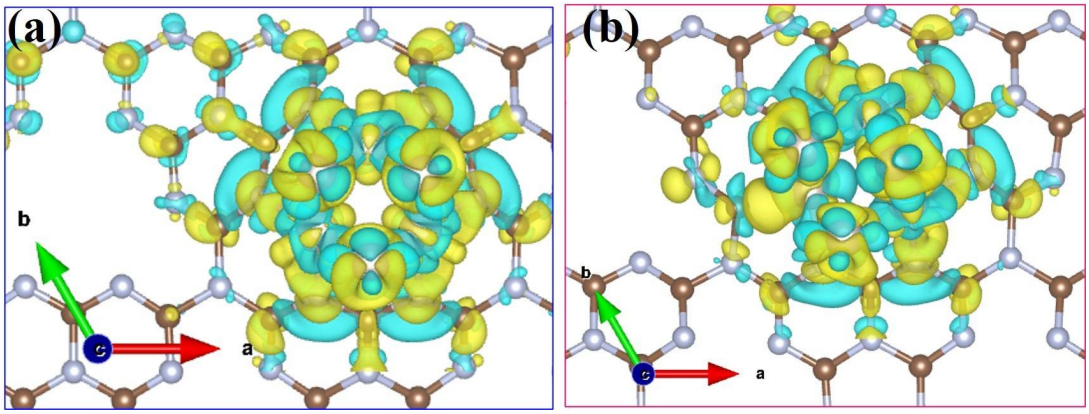

Fig. S28 The charge density difference analysis for (**a**) Ru NCs/C_3N_4 and (**b**) Ru NCs/V_N-C_3N_4. (Yellow and blue contours represent electron accumulation and depletion, respectively).

3 Appendix Table

Table S1 Element analysis results of g-C_3N_4, C_3N_4-Ar, $RuCl_x$-C_3N_4 and Ru NCs/V_N-C_3N_4.

Sample	Repeat	C [%]	N [%]	N/C
g-C_3N_4	#1	34.79	60.89	1.750216
	#2	34.65	60.61	1.749206
	#3	34.63	60.53	1.747906
$RuCl_x$-C_3N_4	#1	24.23	41.99	1.732976
	#2	24.37	42.04	1.725072
	#3	24.31	41.96	1.726039
Ru NCs/V_N-C_3N_4	#1	8.07	13.44	1.665428
	#2	8.6	13.98	1.625581
	#3	7.59	12.77	1.682477
C_3N_4-Ar	#1	34.24	59.87	1.748540
	#2	34.23	59.84	1.748174
	#3	34.11	59.75	1.751686

Table S2 EXAFS fitting parameters at the Ru K-edge for various samples.

Sample	Shell	N [a]	R (Å) [b]	σ^2 (Å^2·10^{-3}) [c]	ΔE_0 (eV) [d]	*R* factor (%)
$RuCl_x$-C_3N_4	Ru-N	2.2	2.09	2.1	-2.8	0.6
	Ru-Cl	3.0	2.38	4.9	6.5	
Ru NCs/V_N-C_3N_4	Ru-N/C	1.7	1.99	1.9	7.9	0.7
	Ru-Ru	6.8	2.68	5.4	5.9	

[a] *N*: coordination numbers; [b] *R*: bond distance; [c] σ^2: Debye-Waller factors; [d] ΔE_0: the inner potential correction. *R* factor: goodness of fit. S_0^2 was set as 0.84/0.88/0.90 for Ru-N/O, Ru-Ru/Ru-Cl, which was obtained from the experimental EXAFS fit of reference RuO_2/Ru foil/$RuCl_3$ by fixing CN as the known crystallographic value and was fixed to all the samples.

Table S3 HER performance comparison of overpotential and Tafel slope with recently developed Ru-based bifunctional electrocatalysts.

Samples	10 mA cm^{-2}	Tafel slope	Ref.
	mV	mV dec^{-1}	
Ru/Co–N–C-800 °C	23	27.8	[24]
CoFeP@Ru	38	21	[25]
Ru@FeCoP	11	31.6	[26]
Ru@B,N-CNTs	54	90	[27]
Ru-FeRu@C/NC	23	23.7	[28]
Ni_3N/Ru/NCAC	42	59	[29]
CoNG/Ru	15	42.9	[30]
RuO_2/Co_3O_4	89	91	[31]
e-$Ni_{0.6}Ru_{0.4}$@C	33	30	[32]
RuO_2-Fe_2O_3/HrGO NSs	239	97	[33]
Ru_1Co_2 NP	188	66.5	[34]
Ru NCs/V_N-C_3N_4	**8**	**24**	**This work**

Table S4 Details about the calculation of mass activity for HER process.

Samples	$RuCl_x$-C_3N_4	Ru NCs/V_N-C_3N_4	Ru/C	RuO_2	Pt/C
$I_{100\ mV}$/mA cm^{-2}	26.5	**448.9**	161.9	102.0	198.6
Loading/mg cm^{-2}	3.0	**3.0**	3.0	3.0	3.0
Content (Ru)/wt%	11.35	**5.57**	5.00	75.95	-
Content (Pt)/wt%	-	**-**	-	-	20.00
The actual loading of noble metals	0.341	**0.167**	0.150	2.279	0.600
Mass activity/A g^{-1}	77.8	**2685.5**	1079.3	44.8	331.0
Mole activity/A mol^{-1}	7865.6	**271504.1**	109117.2	4529.3	64578.1

Table S5 OER performance comparison of overpotential and Tafel slope with recently developed Ru-based bifunctional electrocatalysts.

Samples	10 mA cm^{-2}	Tafel slope	Ref.
	mV	mV dec^{-1}	
Ru/Co–N–C-800 °C	276	65.7	[24]
CoFeP@Ru	340	58	[25]
Ru@FeCoP	212	45.7	[26]
Ru@B,N-CNTs	315	61.5	[27]
Ru-FeRu@C/NC	345	64.7	[28]
Ni_3N/Ru/NCAC	288	60	[29]
CoNG/Ru	350	82.3	[30]
RuO_2/Co_3O_4	305	69	[31]
e-$Ni_{0.6}Ru_{0.4}$@C	250	46	[32]
RuO_2-Fe_2O_3/HrGO NSs	386	67	[33]
Ru_1Co_2 NP	240	54.4	[34]
Ru NCs/V_N-C_3N_4	**200**	**60**	**This work**

Table S6 The value of C_{dl}, ECSA and BET surface area for various samples.

Samples	C_{dl} (mF cm^{-2})	ECSA (cm_{ECSA}^2)	BET surface area (m^2 g^{-1})
$RuCl_x$-C_3N_4	8.8	220	47.6
Ru NCs/V_N-C_3N_4	**49.6**	**1240**	**128.5**
Ru/C	25.0	625	-
RuO_2	27.4	685	-

Table S7 Details about the calculation of mass activity for OER process.

Samples	$RuCl_x$-C_3N_4	Ru NCs/V_N-C_3N_4	Ru/C	RuO_2	Pt/C
$I_{1.6\ V}$/mA cm^{-2}	4.3	401.0	18.1	100.4	12.2
Loading/mg cm^{-2}	3.0	3.0	3.0	3.0	3.0
Content (Ru)/wt%	11.35	5.57	5.00	75.95	-
Content (Pt)/wt%	-	-	-	-	20.00
The actual loading of noble metals	0.341	0.167	0.150	2.279	0.600
Mass activity/A g^{-1}	12.6	2398.9	120.7	44.1	20.3
Mole activity/A mol^{-1}	1273.8	242528.8	12202.8	4458.5	3960.5

Table S8 OWS performance comparison of cell voltage and stability with recently developed Ru-based bifunctional electrocatalysts.

Samples	10 mA cm^{-2}	Stability	Ref.
	mV	Time (h)@10 mA cm^{-2}	
Ru/Co–N–C-800 °C	1.500	15	[24]
CoFeP@Ru	1.760	10	[25]
Ru@FeCoP	1.540	100	[26]
Ru@B,N-CNTs	1.570	40	[27]
Ru-FeRu@C/NC	1.630	50	[28]
Ni_3N/Ru/NCAC	1.550	24	[29]
CoNG/Ru	1.580	10	[30]
RuO_2/Co_3O_4	1.650	11	[31]
e-$Ni_{0.6}Ru_{0.4}$@C	1.520	12	[32]
RuO_2-Fe_2O_3/HrGO NSs	1.860	16	[33]
Ru_1Co_2 NP	1.590	10	[34]
Ru NCs/V_N-C_3N_4	**1.488**	**40**	**This work**

4 References

1. H. A. Gasteiger, N. Markovic, P. N. Ross, Jr. and E. J. Cairns, *The Journal of Physical Chemistry*, 1994, **98**, 617-625.

2. H. A. Gasteiger, N. M. Markovic and P. N. Ross, Jr., *The Journal of Physical Chemistry*, 1995, **99**, 16757-16767.

3. H. A. Gasteiger, N. M. Markovic and P. N. Ross, Jr., *The Journal of Physical Chemistry*, 1995, **99**, 16757-16767.

4. Q. Hu, K. Gao, X. Wang, H. Zheng, J. Cao, L. Mi, Q. Huo, H. Yang, J. Liu and C. He, *Nat. Commun.*, 2022, **13**, 3958.

5. Q. Wang, C.-Q. Xu, W. Liu, S.-F. Hung, H. Bin Yang, J. Gao, W. Cai, H. M. Chen, J. Li and B. Liu, *Nat. Commun.*, 2020, **11**, 4246.

6. D. C. Koningsberger and R. Prins, 1987, **92**.

7. J. J. Rehr and R. C. Albers, *Reviews of Modern Physics*, 2000, **72**, 621-654.

8. B. Ravel and M. Newville, *J. Synchrotron Radiat.*, 2005, **12**, 537-541.

9. W. Kohn and L. J. Sham, *Phys. Rev.*, 1965, **140**, A1133-1138.

10. P. E. Blöchl, *Phys. Rev. B*, 1994, **50**, 17953-17979.

11. G. Kresse and D. Joubert, *Phys. Rev. B*, 1999, **59**, 1758-1775.

12. J. P. Perdew and Y. Wang, *Phys. Rev. B*, 1992, **45**, 13244-13249.

13. G. Kresse and J. Hafner, *Phys. Rev. B*, 1993, **47**, 558-561.

14. G. Kresse and J. Furthmüller, *Phys. Rev. B*, 1996, **54**, 11169-11186.

15. G. Kresse and J. Furthmüller, *Computational Materials Science*, 1996, **6**, 15-50.

16. J. P. Perdew, K. Burke and M. Ernzerhof, *Phys. Rev. Lett.*, 1996, **77**, 3865-3868.

17. S. Grimme, J. Antony, S. Ehrlich and H. Krieg, *J. Chem. Phys.*, 2010, **132**, 154104.

18. Y. Zheng, Y. Jiao, Y. H. Zhu, L. H. Li, Y. Han, Y. Chen, A. J. Du, M. Jaroniec and S. Z. Qiao, *Nat. Commun.*, 2014, **5**, 1-8.

19. J. K. Nørskov, T. Bligaard, A. Logadottir, J. Kitchin, J. G. Chen, S. Pandelov and U. Stimming, *Journal of The Electrochemical Society*, 2005, **152**, J23-J26.

20. J. K. Nørskov, J. Rossmeisl, A. Logadottir, L. Lindqvist, J. Kitchin, T. Bligaard and H. Jonsson, *The Journal of Physical Chemistry B*, 2004, **108**, 17886-17892.

21. D. R. Lide, *CRC press*, 2004, **85**.

22. X. Wang, K. Maeda, A. Thomas, K. Takanabe, G. Xin, J. M. Carlsson, K. Domen and M. Antonietti, *Nat. Mater.*, 2009, **8**, 76-80.

23. J. Lv, L. Wang, R. Li, K. Zhang, D. Zhao, Y. Li, X. Li, X. Huang and G. Wang, *ACS Catal.*, 2021, **11**, 14338-14351.

24. C. Rong, X. Shen, Y. Wang, L. Thomsen, T. Zhao, Y. Li, X. Lu, R. Amal and C. Zhao, *Adv. Mater.*, 2022, **34**, 2110103.

25. S. Liu, X. Mu, P. Ji, Y. Lv, L. Wang, Q. Zhou, C. Chen and S. Mu, *ChemCatChem*, 2020, **12**, 5149-5155.

26. Y. Wang, Y. Du, Z. Fu, J. Ren, Y. Fu and L. Wang, *J. Mater. Chem. A*, 2022, **10**, 16071-16079.

27. M. Fan, X. Chen, M. Zhang, L. Cui, X. He and X. Zou, *Inorg. Chem. Front.*, 2022, **9**, 968-976.

28. W. Feng, Y. Feng, J. Chen, H. Wang, Y. Hu, T. Luo, C. Yuan, L. Cao, L. Feng and J. Huang, *Chem. Eng. J.*, 2022, **437**, 135456.

29. X. Zhao, X. Yong, Q. Ji, Z. Yang, Y. Song, Y. Sun, Z. Cai, J. Xu, L. Li, S. Shi, F. Chen, C. Li, P. Wang and J.-B. Baek, *J. Mater. Chem. A*, 2023.

30. T. He, Y. Peng, Q. Li, J. E. Lu, Q. Liu, R. Mercado, Y. Chen, F. Nichols, Y. Zhang and S. Chen, *ACS Appl. Mater. Inter.*, 2019, **11**, 46912-46919.

31. H. Liu, G. Xia, R. Zhang, P. Jiang, J. Chen and Q. Chen, *RSC Advances*, 2017, **7**, 3686-3694.

32. Q. Yang, P. Jin, B. Liu, L. Zhao, J. Cai, Z. Wei, S. Zuo, J. Zhang and L. Feng, *J. Mater. Chem. A*, 2020, **8**, 9049-9057.

33. H. Mosallaei, H. Hadadzadeh, A. A. Ensafi, K. Z. Mousaabadi, M. Weil, A. Foelske and M. Sauer, *Int. J. Hydrogen Energy*, 2022.

34. Y. Bao, J. Dai, J. Zhao, Y. Wu, C. Li, L. Ji, X. Zhang and F. Yang, *ACS Applied Energy Materials*, 2020, **3**, 1869-1874.